Propagating spatiotemporal activity patterns across macaque motor cortex carry kinematic information

Wei Liang[a,b] (ID), Karthikeyan Balasubramanian[b], Vasileios Papadourakis[b] (ID), and Nicholas G. Hatsopoulos[a,b,1]

Propagating spatiotemporal neural patterns are widely evident across sensory, motor, and association cortical areas. However, it remains unclear whether any characteristics of neural propagation carry information about specific behavioral details. Here, we provide the first evidence for a link between the direction of cortical propagation and specific behavioral features of an upcoming movement on a trial-by-trial basis. We recorded local field potentials (LFPs) from multielectrode arrays implanted in the primary motor cortex of two rhesus macaque monkeys while they performed a 2D reach task. Propagating patterns were extracted from the information-rich high-gamma band (200 to 400 Hz) envelopes in the LFP amplitude. We found that the exact direction of propagating patterns varied systematically according to initial movement direction, enabling kinematic predictions. Furthermore, characteristics of these propagation patterns provided additional predictive capability beyond the LFP amplitude themselves, which suggests the value of including mesoscopic spatiotemporal characteristics in refining brain–machine interfaces.

primary motor cortex | spatiotemporal patterns | propagating activity | kinematic decoding | nonhuman primates

The primary motor cortex (M1) is well known to possess a somatotopic organization such that movement representations of different body parts are segregated spatially across the cortical sheet (1). However, particularly in the upper limb area of M1, the spatial organization is rather crude such that particular limb segment representations are highly distributed and partially overlapping with other limb segment representations (2). Moreover, the somatotopic perspective is a static view of the function of M1 and does not consider both time and space. We have recently demonstrated that spatially organized propagating patterns of excitability signal the initiation of movement but do not specify the details of the particular movement (3, 4). These propagating patterns of excitability were observed in the attenuation of beta oscillation (15 to 35 Hz) amplitude of the local field potential (LFP). Here, we examined high-gamma band (200 to 400 Hz) amplitude prior to movement execution and observed planar propagation in the onset times of high-gamma amplification across different sites in M1. Unlike beta oscillation attenuation propagation, however, the propagating direction of high-gamma amplification times carried kinematic information about the upcoming movement. High-gamma amplitude is known to be a reasonable proxy for multiunit activity (5–7), and, therefore, these results suggest that a spatially organized recruitment order of neural activity across the cortical sheet occurs prior to executing movements, and properties of this recruitment order specify the detailed kinematics of the upcoming movement.

Results

Spatially Organized Amplification in the High-Gamma Envelope upon Movement. Two rhesus macaques (Bx and Ls) were trained to perform reach tasks with their right upper limbs constrained in a 2D exoskeletal robot with the hand holding a joystick. In this reach task, they were required to hold the joystick stably for a length of time (600 ms for Ls and 1,000 ms for Bx) at a center hold target, then move the joystick to one of eight peripheral targets upon presentation of a peripheral target (see the *Inset* in Fig. 1 *A*). The mean (SD) reach duration across trials was 669.8 ms (253.0 ms) and 372.8 ms (162.8 ms) for Bx and Ls, respectively, and mean reaction time was 392.7 ms (85.7 ms) and 186.7 ms (74.9 ms) for Bx and Ls, respectively. While they were performing the task, we recorded MUA and LFPs from two 64-electrode arrays implanted in M1 (see *SI Appendix,* Fig. S1 *Top* panels for implant locations). We filtered LFPs from 200 Hz to 400 Hz and took the amplitude of their Hilbert transform—this is the signal which we refer to as high-gamma envelopes. Trial-averaged high-gamma envelopes were different for different reach directions (Fig. 1*A*), exhibiting directional tuning. Tuning curves for the high-gamma

Significance

Propagating activity patterns including waves are prevalent across cortical areas, but experimental evidence for their role in carrying behaviorally relevant information is rare, and, when present, often reflects the general behavioral state. This work provides the first evidence, to our knowledge, of a spatially organized recruitment order of activity across the motor cortical sheet that informs details of the upcoming movement. Furthermore, characteristics of propagation provide additional predictive power in decoding kinematics beyond information-rich activity amplitudes. The nonredundant movement-specific information exhibited by these propagating patterns not only has scientific implications for the functional organization of motor cortex but also holds potential to aid translational brain–machine interface research.
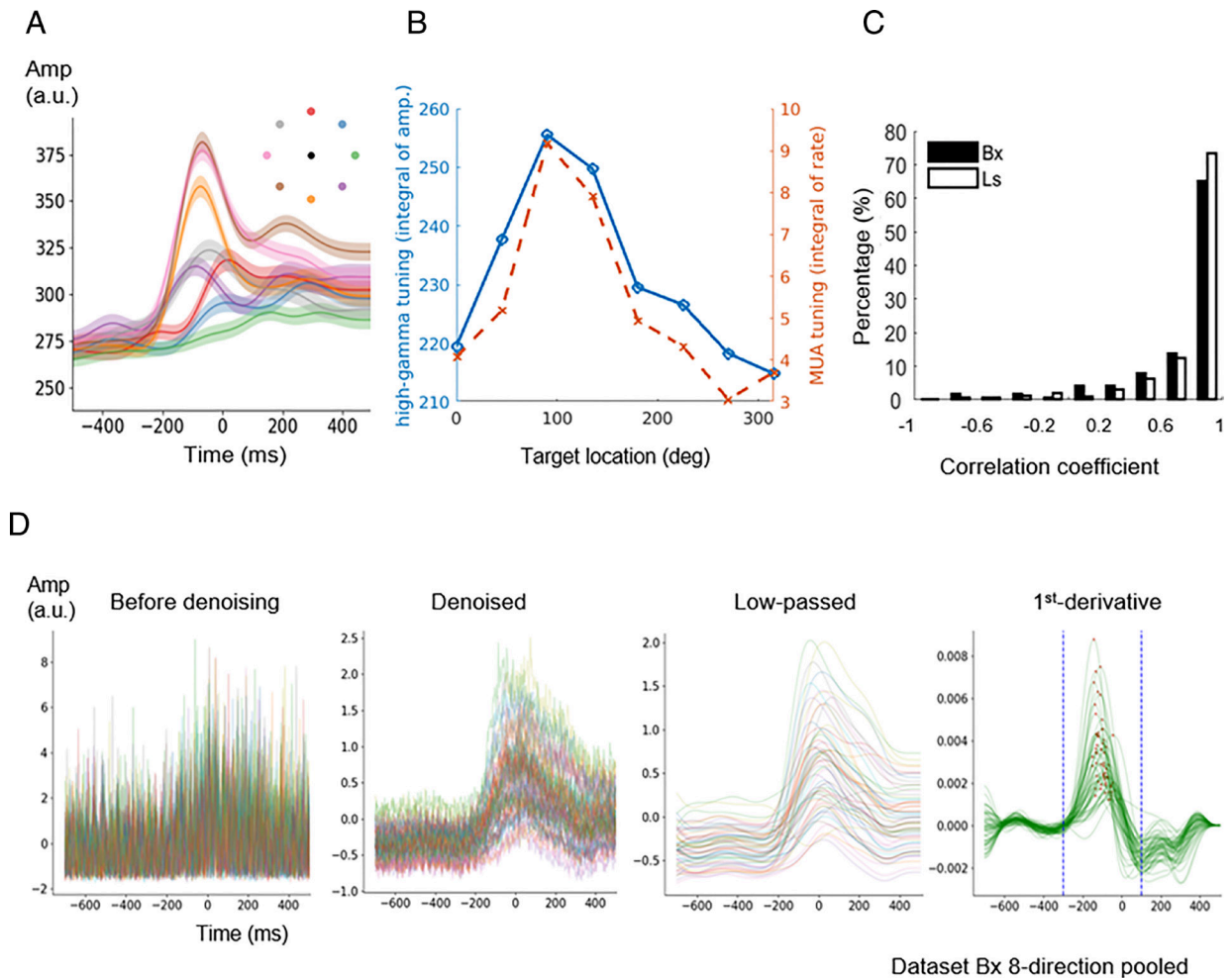
Fig. 1. Processing information-rich high-gamma envelopes. (*A*) Trial-averaged high-gamma amplitude envelopes amplify right before movement onset (0 ms), modulating with target reach directions (targets distinguished by different colors). Results from a representative electrode are shown. Error shades represent SEM. *Inset* shows the target locations in different colors. (*B*) Tuning properties of the high-gamma envelopes (in blue) closely track those of multiunit activities (MUA in orange) on a representative channel. (*C*) Distribution of correlation coefficients between the tuning curves of high-gamma envelopes and tuning curves of MUAs on the same electrodes, for monkey Bx (in black) and monkey Ls (in white). (*D*) Sequential steps for processing single-trial high-gamma envelopes, where each trace represents a single electrode: from left to right, envelopes are z-scored by electrode baselines, then PCA-ed and denoised with an autoencoder, and then low-passed below 5 Hz. The amplification times (red dots) were then determined from the maximums of their first-derivatives (in green) within the time window of interest (blue dotted window).

envelopes and MUA were generally similar in shape for the same electrode (Fig. 1*B* compares turning curves for a representative electrode). We correlated the tuning curves between MUA and high-gamma activity for the same electrodes and found that the mean (SD) tuning correlation was 0.75 (0.35) for Bx and 0.80 (0.29) for Ls (Fig. 1*C*). We also looked at the cross-correlation of MUA and high-gamma activity on a single-trial basis over a wide range of lags. In general, high-gamma activity preceded MUA—the mean (over electrodes) lag at peak correlation for each session ranged from 15.4 to 34.2 ms across sessions for Bx and from 32.6 to 83.3 ms for Ls; the mean peak correlation of the time-series ranged from 0.32 to 0.36 for Bx and from 0.41 to 0.57 for Ls.

While trial-averaged high-gamma envelopes generally exhibited directional specificity and amplification upon movement onset, it was not possible to extract meaningful information from single-trial envelopes because of weak signal-to-noise. Thus, we denoised single-trial envelopes by using a contractive autoencoder (8) and then smoothed the envelopes (Fig. 1*D*) (see *Materials and Methods* for details). Note that all the electrodes at all timepoints were concatenated into a long vector for denoising so that no spatial information was used in the denoising process. The high-gamma envelopes from different electrode locations tended to

amplify around movement initiation but at different times. To precisely quantify the amplification time for each electrode, we took the first derivative of the smoothed envelope and determined the maximum-attaining time within a time window of [–300 ms, 100 ms] relative to movement onset (Fig. 1*D* continued). We computed the median amplification time across electrodes within a trial and then averaged those medians across trials. For Bx, the mean (SD) of the median amplification times relative to movement onset was –120.3 ms (45.6 ms) for the lateral array and –64.4 ms (108.4 ms) for the medial array. For Ls, the mean median amplification time was –81.1 ms (60.0 ms) for the lateral array and –81.5 ms (67.9 ms) for the medial array.

We then sought to characterize the spatial organization of these amplification times across each cortical array by fitting the amplification times to a 2D plane from which three propagating parameters were extracted: the direction of propagation, the speed of propagation, and the fitness (R^2) of the planar fit (Fig. 2 *A*, *Middle* and *Right*). It should be emphasized that the definition of spatial patterning in our work contains only the times of amplification on each electrode and not their amplitudes. To determine statistical significance of the planar fit, we randomly shuffled the locations of the electrodes 500 times for each trial and fit a plane to each shuffle
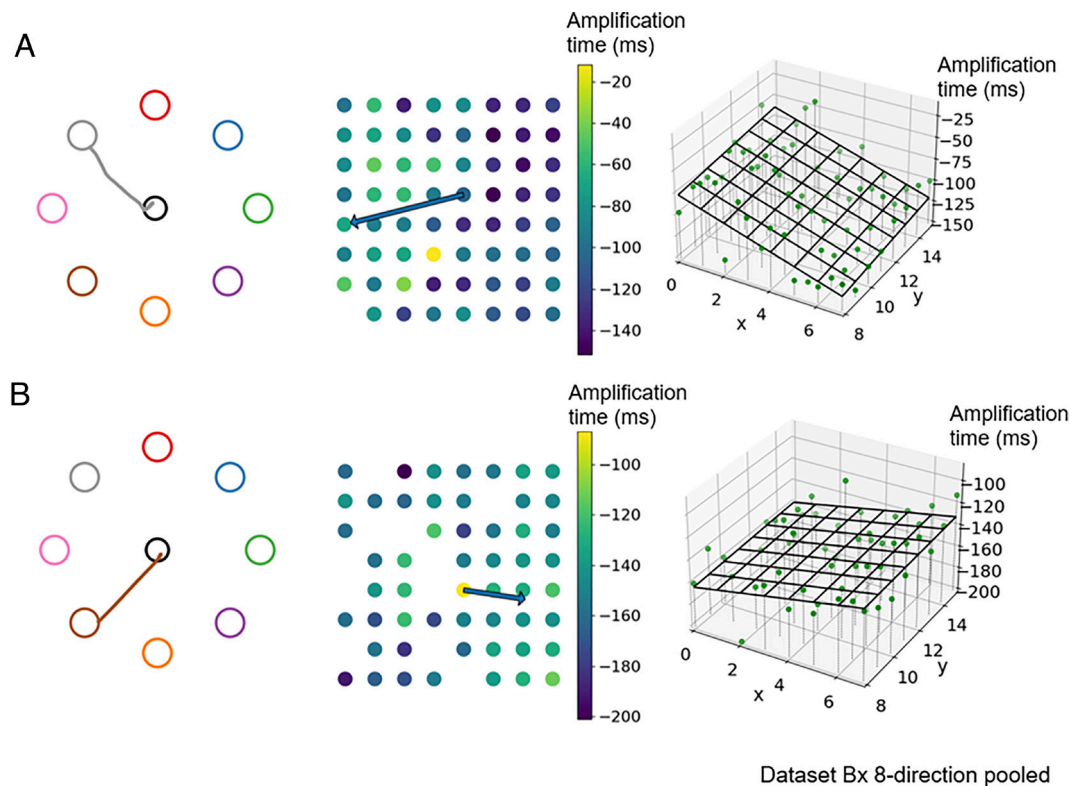
Fig. 2. Single-trial propagation directions were different for different movement directions. (*A* and *B*) are two different trials for monkey Bx. *Left*: movement path plotted on the target map. *Middle*: the amplification times (w.r.t. movement onset) of electrodes from the lateral array were color-coded, with the propagation direction marked with the arrow (the length of the arrow represents the R^2 of the fit: *A*: $R^2 = 0.390$, *B*: $R^2 = 0.210$). *Right*: The amplification times (w.r.t. movement onset) of electrodes from the lateral array were represented as heights of the green dots in a 3D space where x and y axes represent electrode locations. Black grid represents planar fit.

to form an overall distribution of shuffled R^2 values. We determined the significant threshold of R^2 as the top 5 percentile of the shuffled R^2 values—if the actual R^2 exceeded that threshold, we took that as a significant planar propagating pattern (see *Materials and Methods* for details). For the lateral arrays, 1,235 out of 2,460 trials (50%) exhibited significant planar propagation patterns for Bx and 898 out of 1,050 trials (86%) for Ls exhibited significant planar propagation patterns. For the medial arrays, fewer trials exhibited significant planar propagation patterns in general (408 out of 2,460 trials or 17% for Bx and 482 out of 1,050 trials or 46% for Ls).

Movement-Specific Propagation Patterns. As the monkey reached for targets in different directions (Fig. 2 *A* and *B*, *Left*), the propagating directions of the high-gamma envelope varied (Fig. 2 *A* and *B*, *Middle* and *Right*), indicating that there might be movement- or goal-related information expressed in the propagation patterns. There were, in fact, systematic and significant differences in propagation direction ($P < 0.001$ for both monkeys, nonparametric test for common median for multiple groups of angles) across trials with significant planar propagation in the lateral arrays (Fig. 3 *A* and *B*, *Top*). The probability density (*SI Appendix*, Fig. S2 *A*, *Top*) and mean propagating directions for monkey Bx primarily formed two modes (each corresponding to four adjacent reach directions, i.e., 0,45,90,135° targets versus 180,225,270,315° targets; see *Materials and Methods* for target degree assignment), one centered ~210° and one centered ~0° (Fig. 3 *A*, *Bottom*). We also examined the probability density of propagation speed for the significant trials (*SI Appendix*, Fig. S2 *A*, *Bottom*), which also differed by reach directions and followed similar grouping as the propagating directions (see Table 1 for

descriptive statistics of propagation characteristics for Bx). For monkey Ls, the probability densities of propagation direction and speed did not exhibit clear clustering (*SI Appendix*, Fig. S2*B*) although mean propagation directions clustered into two modes albeit not as distinct as with Bx (Fig. 3 *B*, *Bottom*; see Table 2 for descriptive statistics of propagation characteristics for Ls).

The formation of these two modes in the propagation characteristics can be explained by the biased kinematic trajectories generated by the monkeys due to training history. The monkeys were heavily trained on the blue and brown targets; thus, Bx tended to generate initial trajectories for other adjacent reach targets that were clustered around the trajectories of the heavily trained targets. This was evident from the initial mean paths for each target (Fig. 4 *A*, *Top Inset*) and the mean velocity angles for each target (Fig. 4 *A*, *Top*) suggesting that the propagation properties were more closely linked to movement execution rather than the movement goal. The relationship between mean launch angles and mean propagation directions for each target is shown more clearly in Fig. 4 *A*, *Bottom*. For monkey Ls, initial mean kinematic paths (Fig. 4 *B*, *Top Inset*) and mean velocity angles (Fig. 4 *B*, *Top*) also roughly formed two groups (45, 90, 135, and 180° targets versus 225, 270, 315, and 0° targets), which corresponded to the grouping of the propagation directions with the exception of the 45° target (Fig. 4 *B*, *Bottom*).

For the medial arrays, although there was not an obvious correspondence between kinematics groupings and propagation characteristics (Fig. 5 *A* and *B* and *SI Appendix*, Fig. S3), propagation directions were significantly different (or borderline significantly different) across target directions ($P < 0.001$ for Ls, $P = 0.064$ for Bx, nonparametric test for common
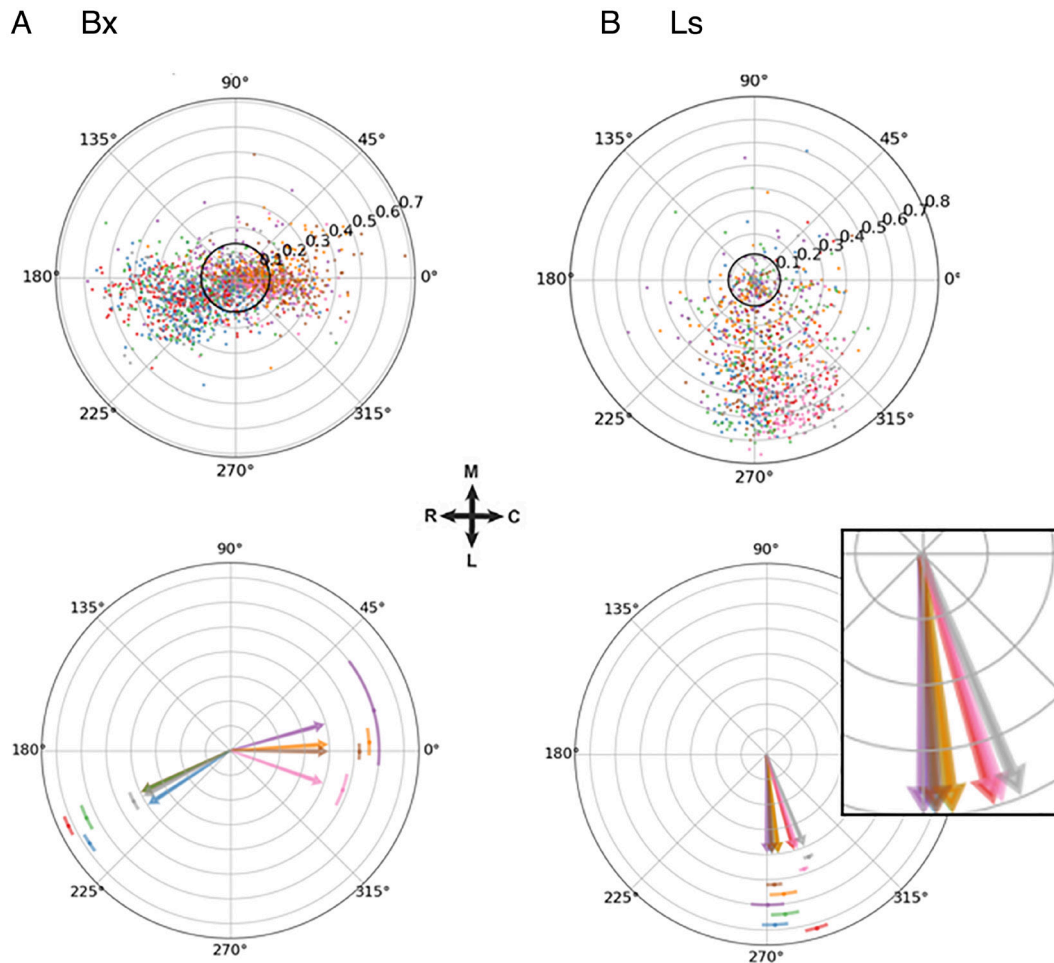
Fig. 3. Summary of single-trial spatiotemporal propagation directions for the lateral arrays. (*A* and *B*) are for Monkey Bx and Ls, respectively. *Top*: polar scatter plot of propagation directions. Each dot is a single trial color-coded by reach direction. Angle represents propagation direction, while radius represents the associated R^2. Black solid circle represents the threshold of significant R^2 values. *Bottom*: summary of propagation directions for significant trials for each reach direction. Angle of arrow represents the mean propagation direction, while the error bar represents the 68.27% CI for the mean. The bottom summary plot in *B* was zoomed in to show details.

median for multiple groups of angles). The descriptive statistics for propagation characteristics can be found in Tables 3 and 4.

Although we examined planar propagation in medial and lateral arrays separately, the propagation characteristics of the lateral array and medial array were not isolated. The propagation speed in the medial array was correlated with the propagation speed in the lateral array for both monkeys (for Bx, Pearson correlation coefficient r = 0.377, P < 0.001, n = 248; for Ls,

r = 0.473, P < 0.001, n = 415, see *SI Appendix*, Fig. S5, *Top*). Also, the median amplification times in the medial array were correlated with the median amplification times in the lateral array for both monkeys (for Bx, Pearson correlation coefficient r = 0.610, P < 0.001, n = 248; for Ls, r = 0.838, P < 0.001, n = 415, see *SI Appendix*, Fig. S5, *Bottom*). These results suggest that the propagating patterns we examined in isolated arrays are part of a more global pattern that extends across the upper limb area of M1.

Table 1.   200 to 400 Hz propagation characteristics of trials with significant planar propagation on the lateral array for monkey Bx

Reach target (deg)	Propagating direction (deg) (mean ± SEM) (r)	Propagating speed (m/s) (mean ± SEM) (median)	Sample size
0	205.0 ± 4.2 (r = 0.67)	0.065 ± 0.004 (0.051)	162
45	213.4 ± 2.8 (r = 0.81)	0.061 ± 0.003 (0.047)	220
90	205.0 ± 2.7 (r = 0.83)	0.052 ± 0.003 (0.037)	212
135	207.7 ± 4.2 (r = 0.66)	0.059 ± 0.003 (0.055)	170
180	340.6 ± 7.2 (r = 0.52)	0.088 ± 0.005 (0.079)	104
225	359.6 ± 2.9 (r = 0.88)	0.098 ± 0.003 (0.094)	162
270	3.7 ± 5.0 (r = 0.68)	0.100 ± 0.004 (0.091)	111
315	15.7 ± 20.8 (r = 0.20)	0.094 ± 0.006 (0.086)	94

SEM is standard error of mean. r is length of the mean resultant vector of angles, which is a measure of concentration.

Table 2. 200 to 400 Hz propagation characteristics of trials with significant planar propagation on the lateral array for monkey Ls

Reach target (deg)	Propagating direction (deg) (mean ± SEM) (r)	Propagating speed (m/s) (mean ± SEM) (median)	Sample size
0	276.7 ± 4.4 (r = 0.74)	0.078 ± 0.004 (0.072)	113
45	272.9 ± 3.8 (r = 0.81)	0.084 ± 0.003 (0.081)	120
90	286.1 ± 3.1 (r = 0.88)	0.085 ± 0.003 (0.082)	134
135	292.3 ± 1.7 (r = 0.95)	0.084 ± 0.002 (0.081)	132
180	288.0 ± 1.4 (r = 0.97)	0.079 ± 0.002 (0.078)	123
225	273.4 ± 2.7 (r = 0.91)	0.089 ± 0.004 (0.085)	88
270	277.0 ± 4.9 (r = 0.71)	0.075 ± 0.004 (0.068)	100
315	270.5 ± 5.6 (r = 0.67)	0.071 ± 0.004 (0.067)	88

SEM is standard error of mean. r is length of the mean resultant vector of angles, which is a measure of concentration.

Decoding Kinematics with Propagation Patterns. Given the relationship between kinematics and propagation patterns observed above, we set out to test if that relationship could be useful in kinematic decoding. We used propagation parameters (propagation direction, propagation speed, and planar regression goodness-of-fit, R^2) from both arrays to decode hand velocity at particular times with generalized linear models (GLMs). We built a different model for each time point relative to movement onset, as there existed only one set of propagation parameters for each trial, and we sought to determine where in time over the trial these propagating parameters best predicted the hand velocity. For monkey Bx, the fraction of variance explained (or R^2) of this prediction (plotted in red) reached a peak average R^2 of 0.427 at 100 ms, which was significantly better than shuffled control ($P = 0.001$ for single-tailed Wilcoxon test, w = 0.0; Fig. 6 *A*, *Top*); in other words, the spatiotemporal variables were most predictive of velocities at 100 ms after movement onset for Bx. For monkey Ls, the fraction of variance explained of this prediction (in red) reached a peak average R^2 of 0.268 at 40 ms, which was
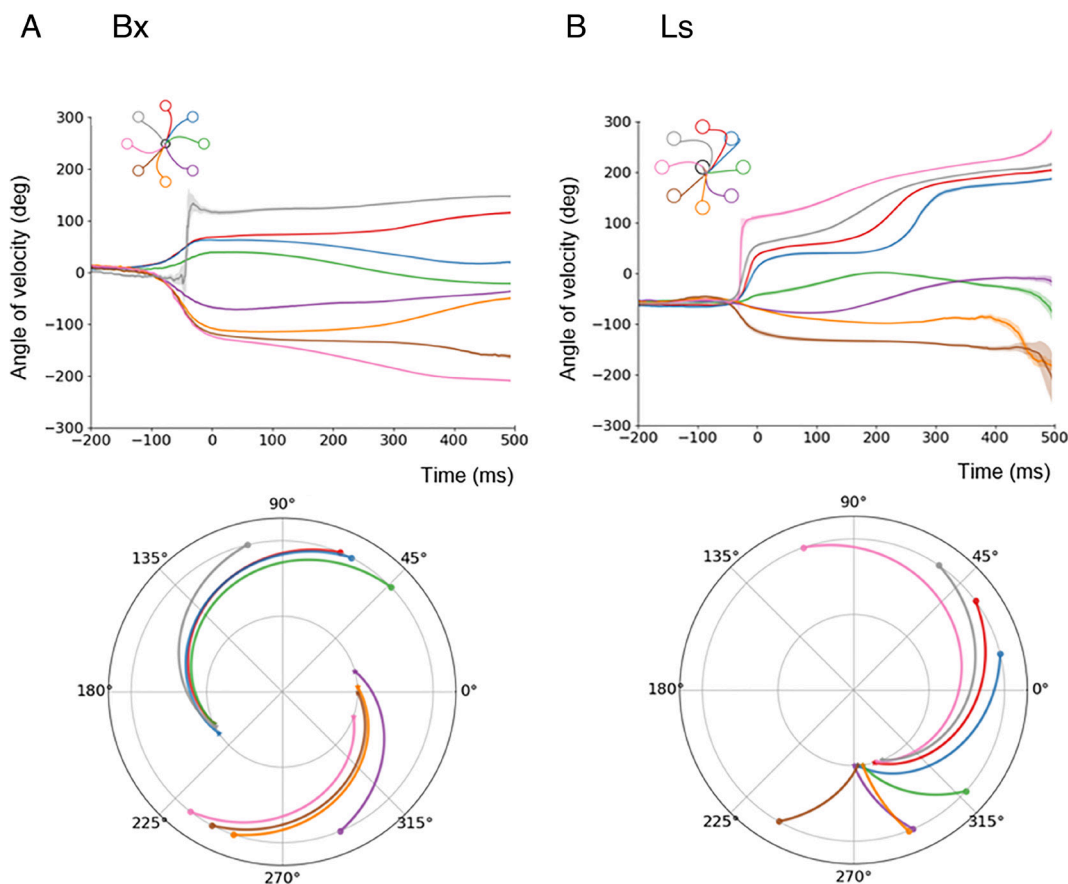
Fig. 4. Clustering of hand kinematics and corresponding propagation directions for the lateral arrays. (*A* and *B*) are for Monkey Bx and Ls, respectively. *Top*: mean angle of velocity traces across time w.r.t. movement onset (error shade represents the 68.27% CI for the mean). The mean hand paths are shown in the *Inset*. Colors represent different targets. *Bottom*: stars on the inner circle represent mean propagation directions for each reach target, while dots on the outer circle represent mean launch direction at movement onset (0 ms) for each reach target. The lines connecting the inner and outer dots were linearly interpolated for visualization purposes. Clusters of propagation directions correspond to clusters of kinematic launch directions for all targets in both monkeys, except for the blue direction in Ls (*B*).

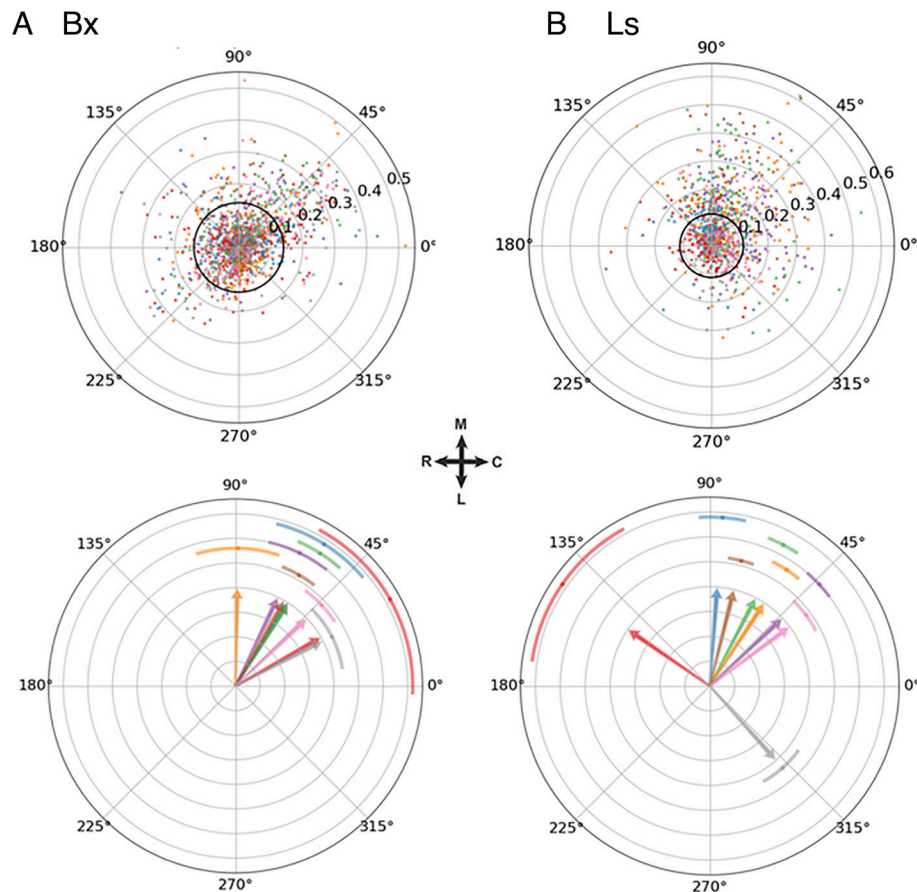**Fig. 5.** Summary of single-trial spatiotemporal propagation directions for the medial array. (*A* and *B*) are for Monkey Bx and Ls, respectively. *Top*: polar scatter plot of propagation directions. Each dot is a single trial color-coded by reach direction. Angle represents propagation direction, while radius represents the associated R^2. Black solid circle represents the threshold of significant R^2 values. *Bottom*: summary of propagation directions for significant trials of each reach direction. Angle of arrow represents the mean propagation direction, while the error bar represents the 68.27% CI for the mean.

significantly better than shuffled control ($P = 0.001$ for single-tailed Wilcoxon test, w = 0.0; Fig. 6*B*).

Next, we looked at the contributions of each type of propagating parameter by using each separately to predict velocities. For Bx, models using only propagation direction reached performance levels nearly as good as the complete set of parameters, and R^2 also had some predictive power (Fig. 6 *A*, *Bottom*). For Ls, models using propagation direction parameters only and using R^2 only both had similar predictive power, though not as good as the complete set (Fig. 6 *B*, *Bottom*). For both monkeys, the propagation speed lacked predictive power when used alone. These consistent prediction results across monkeys indicated that despite the different extents of spread in the propagation parameters, the spatial patterns

provided meaningful kinematic information regarding velocity. It might be argued that the propagation patterns were, in fact, predicting movement speed rather than velocity, and our prediction of velocity could be accounted for by a potential link between movement speed and velocity. However, in this task, movement speed only weakly accounted for movement velocity (the composite R^2 using instantaneous speed to predict instantaneous velocity was 0.03 for Bx and 0.16 for Ls, which were much lower than the performance of velocity prediction using spatial variables for the majority of time points in Fig. 6).

High-gamma band amplitude is known to carry rich kinematic information and has been used in online and offline motor output decoding (5–7, 9). Thus, we wanted to test whether characteristics

Table 3.   200 to 400 Hz propagation characteristics of trials with significant planar propagation on the medial array for monkey Bx

Reach target (deg)	Propagating direction (deg) (mean ± SEM) (r)	Propagating speed (m/s) (mean ± SEM) (median)	Sample size
0	57.6 ± 8.5 (r = 0.58)	0.229 ± 0.021 (0.205)	56
45	58.1 ± 17.2 (r = 0.35)	0.199 ± 0.022 (0.167)	44
90	29.6 ± 31.7 (r = 0.18)	0.170 ± 0.018 (0.157)	54
135	27.3 ± 17.3 (r = 0.30)	0.187 ± 0.015 (0.167)	61
180	43.4 ± 9.7 (r = 0.57)	0.223 + 0.017 (0.238)	45
225	60.3 ± 7.6 (r = 0.66)	0.210 ± 0.017 (0.200)	52
270	89.1 ± 16.8 (r = 0.33)	0.186 ± 0.018 (0.145)	51
315	64.4 ± 12.0 (r = 0.48)	0.198 ± 0.020 (0.160)	45

SEM is standard error of mean. r is length of the mean resultant vector of angles, which is a measure of concentration.

Table 4. 200 to 400 Hz propagation characteristics of trials with significant planar propagation on the medial array for monkey Ls

Reach target (deg)	Propagating direction (deg) (mean ± SEM) (r)	Propagating speed (m/s) (mean ± SEM) (median)	Sample size
0	62.5 ± 5.4 (r = 0.68)	0.133 ± 0.006 (0.129)	92
45	85.7 ± 7.4 (r = 0.65)	0.156 ± 0.008 (0.155)	57
90	145.3 ± 26.2 (r = 0.31)	0.148 ± 0.012 (0.160)	25
135	311.6 ± 11.6 (r = 0.63)	0.167 ± 0.013 (0.174)	25
180	36.7 ± 8.3 (r = 0.64)	0.182 ± 0.010 (0.175)	47
225	76.0 ± 5.1 (r = 0.84)	0.133 ± 0.008 (0.120)	60
270	56.9 ± 5.9 (r = 0.65)	0.111 ± 0.007 (0.097)	89
315	43.1 ± 5.7 (r = 0.68)	0.099 ± 0.006 (0.104)	87

SEM is standard error of mean. r is length of the mean resultant vector of angles, which is a measure of concentration.

of the spatiotemporal propagation patterns contain additional non-redundant kinematic information beyond the high-gamma amplitude envelopes themselves. For this purpose, we compared the performance of three types of models: a) an instantaneous envelope-amplitude-only model; b) a propagation-parameter-only model (including both first-order parameters and second-order interactions); and c) instantaneous amplitude envelope + propagation parameter model. With these models, we then decoded hand velocity continuously throughout the trial. Thus, we had to determine the optimal lag between the continuous amplitude envelope and

continuous hand velocity which occurred at –180 ms and –120 ms for Bx and Ls, respectively, indicating that envelope led the hand velocity as expected in M1 (Fig. 7 *A* and *B*, *Top*). At those optimal lags, the performances of the amplitude envelope + propagation parameter model were significantly better than the envelope-amplitude-only model ($P = 0.001$ for single-tailed Wilcoxon test, w = 0.0 for both monkeys). A trial-shuffling procedure also demonstrated a significant increase in decoding performance when including the propagation parameters to the amplitude envelopes (Fig. 7 *A* and *B*, *Bottom*). These results demonstrate that the spatiotemporal
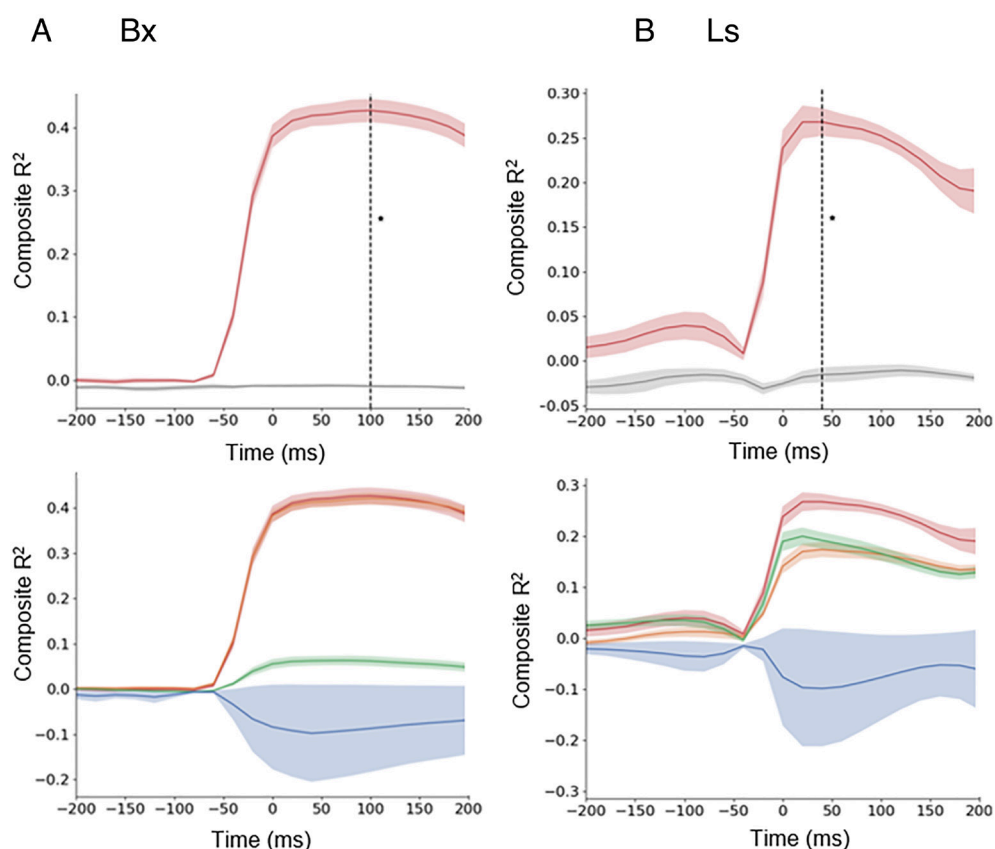

Fig. 6. Propagation parameters can be used to decode hand velocities. (*A* and *B*) are for Monkey Bx and Ls, respectively. *Top*: Prediction performance (composite R^2) for hand velocities at different time points w.r.t. movement onset using all propagation parameters (i.e., propagation direction, speed and planar fitness from both arrays), where a different model was built for each time point. Red traces represent actual performance, and gray line represents performance from the trial-shuffled control. Error shade represents SEM from 10 folds. Optimal time where velocity prediction achieves best results is marked with the dotted vertical line (100 ms in Bx and 40 ms in Ls). Star denotes that propagation parameters can predict kinematics significantly better than chance at the optimal time point from single-tailed Wilcoxon test. *Bottom*: breakdown of contributions from individual propagation parameters on hand velocity prediction. Red trace—all parameters as above; orange trace—propagation direction only; green trace—planar fitness only; blue—propagation speed only. For both monkeys, propagation direction and planar fitness were more useful than propagation speed when used alone to predict movement velocities. For Bx, the red and orange traces largely overlapped.

organization of these high-gamma envelopes provide additional, nonredundant kinematic information beyond the envelope magnitudes alone.

Movement-Specific Propagating Patterns in MUA Encode Kinematics. Our choice of using the high-gamma LFP to analyze spatiotemporal patterning was motivated by the fact that it served as a useful proxy for MUA activity, and it was present on all electrodes to allow for adequate spatial coverage. In contrast, MUA activity was not consistently present on all electrodes. Moreover, some electrodes had sparse MUA activity (defined as average firing rate below 1 Hz throughout movement even for the most modulated direction). This was particularly true for Bx where a quarter of electrodes had sparse MUA activity. Here, we aimed to replicate our findings using MUA activity from Ls where only ~4% of electrodes had sparse MUA activity. For Ls, the mean (SD) median MUA amplification time was −55.3 ms (31.6 ms) for the lateral array and −15.4 ms (43.3 ms) for the medial array. These amplification times were later than the amplification times of the 200 to 400 Hz high-gamma signal (−81.1 ms (60.0 ms) for the lateral array and −81.5 ms (67.9 ms) for the medial array), consistent with the cross-correlation lag between the two signals discussed above.

Next, we computed propagation patterns based on MUA for Ls. For the lateral array, 572 out of 1,167 trials (53%) exhibited significant planar propagation patterns. For the medial array, 205 out of 1,167 trials (18%) exhibited significant planar propagation patterns. These proportions of significant propagations were substantially smaller compared to the corresponding proportions from 200 to 400 Hz signal (86% and 46%). Propagation directions were significantly different across target directions ($P < 0.001$ for both arrays in Ls, non-parametric test for common median for multiple groups of angles). Although propagation directions were similar to those using the high-gamma signal only for certain directions, the global distribution of propagation directions was largely similar when considering all trials. The speed of MUA propagation was in general lower than high-gamma propagation (especially for the medial array).

For those trials exceeding the R^2 threshold, planar propagation fits were generally worse than those for the high-gamma signal, which might have led to lower propagation speed (*SI Appendix*, Fig. S7 and Tables S1 and S2 for more details on the propagation patterns).

Kinematic decoding using MUA propagation parameters was also evident (*SI Appendix*, Fig. S8) and, in fact, was moderately better than when using their high-gamma counterparts. The highest kinematic prediction performance using first-order spatial parameters of MUA was a composite R^2 of 0.332 instead of 0.268 from the high-gamma signal (a 24% increase in performance). Decoding performance using both MUA firing rates and associated spatial variables (first and second order) was slightly better than when using the high-gamma envelopes and their associated spatial variables, with a ~0.06 increase in composite R^2 (a 9% increase in performance).

Discussion

Despite extensive evidence of traveling waves and, more generally, propagating spatiotemporal patterns in cortex (3, 10–19), experimental evidence for their role in carrying behaviorally relevant information is rare, and, when present, often reflects general behavioral state. At the macroscopic scale, forward-directed waves in the 8 to 13 Hz band of human EEG have been documented to propagate from occipital to frontal lobes during visual processing while backward-directed waves from frontal to occipital lobes occur in the absence of sensory input (20). Forward- and backward-directed waves measured in the 2 to 13 Hz band of human ECoG recordings tend to correspond to the encoding and retrieval stages of episodic memory tasks, respectively (21). However, in these cases, wave direction does not provide detailed information about the visual stimulus identity or memory content.

At the mesoscopic scale, traveling phase waves mediated by beta oscillations in M1 propagate in a stereotyped fashion along a rostro-caudal axis in nonhuman primates (22, 23). While it was
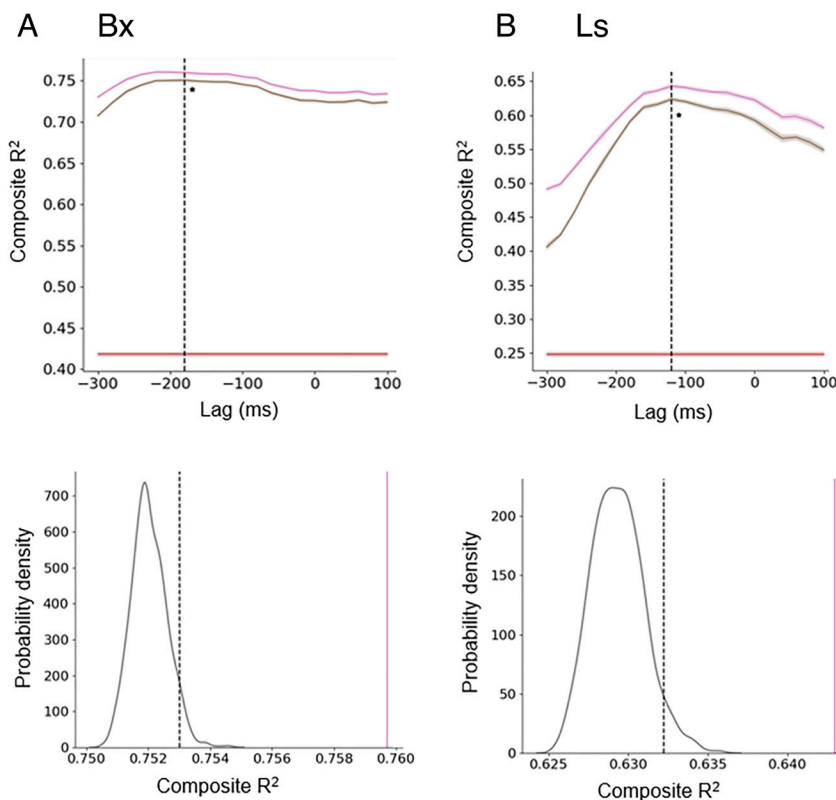

Fig. 7. Propagation parameters provided additional decoding performance on top of amplitude envelopes. (*A* and *B*) are for Monkey Bx and Ls, respectively. Propagation parameters here include not only first-order parameters but also second-order interactions terms. *Top*: prediction performance (composite R^2) for hand velocities at different lags from the instantaneous amplitude envelope (negative lags mean neural signals precede hand velocity), where brown trace denotes using instantaneous envelopes only as predictors; red trace denotes using propagation parameters only (first and second orders) as predictors (performance was lag-independent as there was only one set of spatial variables for the whole trial); pink trace denotes using both instantaneous envelopes and propagation parameters as predictors. Error shade denotes SEM from 10 folds. The time lag where the best mean envelope-amplitude-only performance was achieved was marked by the dotted vertical line (−180 ms for Bx and −120 ms for Ls). Star denotes that amplitude + propagation (pink) achieves significantly better prediction than amplitude-only (brown) at the best lag using a single-tailed Wilcoxon test. *Lower*: the improved performance from including the propagation parameters together with the amplitude envelopes could not be obtained by merely adding propagation parameters from a random trial. The gray distribution shows the decoding performances of random additions of propagation parameters from other trials together with the correct envelopes, with the top 5% threshold marked in dotted vertical black line. The solid pink vertical line denotes the real performance (i.e., addition of corresponding propagation parameters), which exceeds the dotted black line for both monkeys.

found that information about reach target was larger in sequential activity of pairs of neurons whose spatial orientation on the cortical sheet matched the traveling wave axis, characteristics of the waves including their direction and speed did not vary with behavior (23). Moreover, traveling waves mediated by beta oscillations in area V4 have been shown to be triggered by saccadic eye movements (12). While the wave amplitude correlated with the saccade direction, the propagation direction remained invariant propagating from foveal to peripheral locations. Spontaneous traveling waves in the middle temporal area (commonly known as area MT) of marmosets have been shown to improve target detection by temporally aligning a highly excitable state in the receptive field of the target but again wave propagation direction did not carry information about perceptual sensitivity (24).

In this study, we demonstrate, for the first time to our knowledge, a link between neural propagation direction and specifics of movement behavior. We showed that the propagation direction of high-gamma band recruitment timing carries kinematic information by demonstrating that hand launch velocity (and potentially later movement kinematics, see supplementary material including *SI Appendix*, Fig. S6) can be decoded on a trial-by-trial basis. Moreover, the fact that spatially organized propagation patterns provided additional predictive power in decoding kinematics beyond the high-gamma LFP amplitudes (or MUA firing rate) themselves may have implications for improving brain–machine interfaces. Previous offline decoding studies have used high-frequency LFP amplitudes to decode movements and have found that the decoding performance of kinematics and muscle activity was nearly equal to that of spikes (5–7). However, these studies did not consider the spatiotemporal organization of high-frequency LFP amplitude modulation.

More importantly, these findings have fundamental scientific implications as they suggest that there is a dynamic spatial organization of activity on the motor cortical sheet that may serve a functional role in executing movements that goes beyond the static view of somatotopy (1, 2). Given that high-gamma LFP amplitude serves as a close proxy to MUA, these results imply that there is an orderly recruitment sequence of activity across the motor cortical sheet that informs details of the upcoming movement. In fact, we were able to replicate the same analyses with MUA in monkey Ls and found that MUA propagation patterns contained movement-specific spatiotemporal organization that was useful for kinematic decoding. In contrast, propagation direction of beta frequency amplitude attenuation provides no information about upcoming movement kinematics (*SI Appendix*, Fig. S4) and only signals movement initiation in a condition-independent manner (3, 4, 25); we also examined an alternative definition of high-gamma using a lower 100 to 200 Hz frequency band, where we also found propagation patterns, but they provided only limited kinematic information (*SI Appendix*).

In order to extract and characterize single-trial propagation patterns, a number of preprocessing steps were required. First of all, despite the obvious amplitude envelope amplification on trial-averaged data, high-gamma amplitude was too noisy to reliably extract amplification signatures on a single-trial basis. To robustly denoise single trials given the constraint of limited trial counts, we used a combination of principal components analysis (PCA) followed by an autoencoder. A pure autoencoder denoising method was prone to getting stuck at local minima resulting in poor reconstruction, while a pure-PCA denoising method was poor at rejecting severe noise due to lack of a nonlinearity transformation. In the whole denoising process, no spatial information was provided, thus eliminating the possibility of introducing any spatial smoothness. Second, to identify the amplification time on each channel, we chose the time point where

the first derivative of the cleaned envelope reached its maximum thus avoiding the use of an arbitrary threshold on the envelope. Third, after excluding outlier channels (see *Materials and Methods*), we fit a plane to the amplification times in order to compute its propagation properties. The use of a planar fit served as a local approximation to make propagations more tractable, but we acknowledge the possibility that this local pattern could be part of a larger pattern that might be more complex (e.g., rotary or spiral). In fact, when looking at both the lateral and medial arrays simultaneously, the speeds of the two propagating patterns were significantly correlated in both monkeys with the propagation speed of the medial array being approximately twice of that of the lateral array (*SI Appendix*, Fig. S5). Moreover, the amplification times across both arrays were significantly correlated in both monkeys. Although beyond the scope of the current study, this suggests the potential of more complex propagation patterns at a larger spatial scale.

The exact propagation directions differed across the two monkeys particularly on the lateral arrays. This is likely due to the differences in the exact placement of the arrays and individual cerebral organization. Intracortical microstimulation of sites on the lateral array for Bx evoked either hand or wrist movements, while the majority of sites on the lateral array for Ls evoked hand movements (*SI Appendix*, Fig. S1). As explained above, the patterns we observed from single arrays were most likely part of larger spatiotemporal patterns; thus, propagating directions would naturally be different if the spatial windows were slightly shifted, even if the larger patterns were generally similar. Another possible reason for the difference across the two monkeys is the fact that electrode lengths in Bx were 1.5 mm whereas in Ls they were 1.0 mm. The longer electrodes may have reached the upper portion of layer 5, whereas the shorter electrodes were likely in layers 2/3. Nevertheless, despite the individual differences in propagation patterns, these patterns both provided meaningful kinematic decoding in our two monkeys.

In future studies, we plan on extending this investigation to more complex movements with multiple submovements such as sequential movements that are either planned or unplanned. We hypothesize that there should be multiple distinct propagation patterns in the high-gamma band associated with each submovement, especially in the unplanned case.

Materials and Methods

Electrophysiology. Neural recordings were collected from two male rhesus macaques (*Macaca Mulatta*), Bx and Ls. They were each implanted with a set of dual 64-electrode Utah multielectrode arrays (Blackrock Microsystems) in the left primary motor cortex (*SI Appendix*, Fig. S1). The electrode lengths were 1.5 mm for Bx and 1 mm for Ls, with a uniform interelectrode distance of 400 μm in the 8-by-8 grid. The arrays corresponded to the arm/hand areas of the limb trained for the task, as confirmed by electrically stimulating the cortex during surgery with surface electrodes and observing corresponding twitches prior to array implantation. All procedures regarding surgery, animal training, and data collection were approved by the University of Chicago Institutional Animal Care and Use Committee and obey the Guide for the Care and Use of Laboratory Animals.

Behavioral Task. The animals were trained to perform a reach task in different directions with their right upper limb constrained by a 2D exoskeletal robot (BKIN Technologies). All the reach directions were on a horizontal plane roughly at the height of their elbows when their upper limbs were naturally hanging. They performed the task by moving the joystick at the tip of the robot, while receiving simultaneous visual feedback of the cursor position on the screen in front of them. The task involves a hold period (600 ms for Ls and 1,000 ms for Bx) during which the animal held the joystick steadily keeping the cursor within a central target. The peripheral target then appeared indicating the desired reach location. The animal moved the joystick to direct the cursor to the peripheral target. Each target had a radius of 1 cm for Ls and 0.75 cm for Bx; the distance

from the central target to the peripheral target was 6 cm For Ls and 5.5 cm for Bx. The peripheral target could appear in one of 8 possible locations on a circle (in 45° intervals counterclockwise from 0° to 315°, where rightward movement was 0° and forward movement was 90°). A trial was considered successful once the cursor reached the peripheral target and remained in the target for a period of time (100 ms for Ls, 400 to 600 ms for Bx), upon which the animal received juice reward. In total, there were 3 sessions for each monkey.

Data Collection and Preprocessing. Neural signals were collected with Blackrock Microsystems, bandpass filtered from 0.3 Hz to 7.5 kHz with a Butterworth filter and then digitized at 30 kHz. For LFPs, the 30 kHz signal was further low-pass filtered below 500 Hz with a Butterworth filter and downsampled to 2 kHz. For MUA, the 30 kHz signal was high-passed above 250 Hz with a Butterworth filter and threshold crossing events were found when the voltage crossed negative 5.5 times of the RMS.

Extracting Signals from High-Gamma Band and Beta Band. From the 2 kHz LFPs, the high-gamma band signals were extracted by bandpass filtering within 200 Hz to 400 Hz with a Butterworth filter; the beta band signals were extracted by bandpass filtering within a monkey-specific range that corresponded to individual peak frequencies in the beta band power spectrum (18 to 24 Hz for Ls and 28 to 34 Hz for Bx). All band-pass filters had zero-phase distortion. From those band-pass-filtered signals, we computed the Hilbert transformation to obtain the amplitude envelopes. Individual trials were aligned on movement onset defined as the time point where 15% of the peak speed was reached for that trial.

Comparison of High-Gamma Band versus MUA. The MUAs from different trials were aligned on movement onset and binned in 1 ms windows, after which moving averages were computed in sliding windows of 150 ms (in steps of 1 ms). The high-gamma signal used for comparison with MUA was low-passed below 10 Hz to match the smoothing of the MUA. Then, we compared the similarity of the two signal types based on the correlation of tuning curves and cross-correlation of single-trial activity.

Presence of modulation: for each signal type, the mean time-resolved activity was computed for each peripheral target for each electrode. For each electrode and each target direction, the baseline mean and SD was computed over a time window of −700 to −250 ms with respect to movement onset. If the average activity deviated from the baseline mean by at least three SDs at any time point between −200 ms to 500 ms (with respect to movement onset) for any target direction, then we considered this electrode to be modulated.

Robust firing: for MUA, the mean time-resolved activity was computed for each peripheral target for each electrode. If the maximal instantaneous average firing rate exceeded 1 Hz at any time point between −200 ms to 500 ms (with respect to movement onset) for any target direction, then we considered this electrode to have robust firing.

Correlation of tuning curves of MUA and high-gamma activity: for each signal type, the mean time-resolved activity was computed for each peripheral target for each electrode, and the modulation strength for each target direction was determined by the integral of activity between −200 ms to 500 ms with respect to movement onset. The tuning curve was composed of eight modulation strengths, one for each target direction. The Pearson correlation between tuning curves of high-gamma and MUA was computed for each electrode that was modulated and had robust firing.

Cross-correlation of single-trial MUA and high-gamma activity: for each electrode that was modulated and had robust firing, the Pearson correlation between the two signal types was computed within a wide range of lags from −600 ms to 600 ms in steps of 5ms.

Computation of Circular Statistics. Descriptions of propagation directions and movement directions require proper treatments of angular variables. We computed angular means, medians and SEM based on (26–28), implemented in the pycircstat package in python (https://github.com/circstat/pycircstat/tree/master/pycircstat). Briefly, the angular mean is the direction of the mean of the vectors (cos(α_i), sin(α_i)), where α_i represents each angle in the distribution. The angular median is the angle which has the minimum total distance to all other angles in the distribution (in the case of even number of samples, it's the mean of the two angles with the minimal distance). The circular SEM is computed by halving the 68.27% CI of the mean estimation–it only exists when data have enough concentration around the mean (in ref. 28, Equations 26.23-26).

As for statistical tests for multisample analysis of circular data (e.g., different groups of propagation directions), we tested whether different groups of angles shared a common median, using a test suggested by Fisher (26). This is a nonparametric test, serving as a circular analog of the Kruskal–Wallis test (29). It was implemented with the same pycircstat package mentioned above.

Processing Steps for Denoising Single-Trial Activities. Given the temporal variability of high-gamma band and beta band amplitudes on individual trials, a series of steps were performed to denoise single-trial amplitudes. First, trials from multiple daily sessions of the same task of the same monkey were pooled together. For each pooled dataset, only trials with a reaction time within a canonical range were kept (200 to 600 ms for Bx and 0 to 400 ms for Ls), to ensure relative homogeneity of the behaviors. Next, we randomly divided the trials into a training set (90%) and a test set (10%). Then, we z-scored the activities for each electrode with signal mean and SD from the baseline period of the training set (baseline period was defined as −700 ms to −400 ms relative to movement onset for high-gamma and −900 ms to −600 ms for the beta band, during which signals were relatively steady on average). Then, we rearranged the training data to form a 2D matrix (where all timepoints of all electrodes of one trial were flattened into one long column vector and different columns represented different trials) and reduced the dimensionality from 307,328 (128 electrodes × 2,401 time points) to 200 with PCA (accounting for 30.7 to 39.4% of total variance). We applied the same transformations to the test set (accounting for 13.0 to 15.5% of total variance). This PCA step was used to reduce the number of parameters for later training of neural networks. We experimented with more principal components with this PCA step (400 and 800 components) – while they accounted for more total variance in the training set (40.6 to 59.1% with 400 components and 58.2 to 91.5% with 800 components), the total variance accounted for in the test set only increased minimally (13.8 to 16.3% with 400 components and 15.1 to 17.8% with 800 components), and the final denoising performance remained similar. We decided to go with 200 components primarily due to the limited trial count we had for training the later neural network.

To denoise the signal, we used a variant of autoencoders called the contractive autoencoder (8) (implemented in Tensorflow with adaptions from https://github.com/zaouk/contractive_autoencoders). Briefly, the contractive autoencoder aims to reconstruct each 200-dimensional trial vector $\textbf{\textit{Env}}_{\textbf{\textit{reduced}}}$ faithfully through operations of three hidden layers while reducing the sensitivities of the hidden layer representations with respect to the inputs (the latter is termed "Jacobian loss") (see Eqs. **1** and **2**: Eq. **1** describes the total loss as a weighted sum of the reconstruction loss and Jacobian loss, while Eq. **2** spells out the Jacobian loss to be the squared partial derivatives of the hidden layer activities with respect to the inputs). The autoencoder was fitted with a 2:1 cross-validation scheme for early stopping using the 90% training set and then evaluated on the 10% test set. Results reported here were obtained with the following hyperparameters: tradeoff between Jacobian loss and reconstruction loss $\lambda = 0.1$, learning rate = 0.0001, and batch size = 8; hidden layers sizes were 100, 50, and 100, with sigmoid transfer functions used in the encoder (f, for contraction) part and linear functions used in the decoder (g, for expansion) part of the autoencoder. This set of parameters was chosen to achieve a relatively proper level of compression and stable denoising, and the denoising performance and downstream results were quite stable across a wide range of hyperparameters we experimented. All bolded variables in this manuscript denote vectors (for example, input vector $\textbf{\textit{Env}}_{\textbf{\textit{reduced}}}$ here).

$$Loss_{total} = \sum \left(Loss_{recon} \left(\textbf{\textit{Env}}_{\textbf{\textit{reduced}}}, g \left(f \left(\textbf{\textit{Env}}_{\textbf{\textit{reduced}}} \right) \right) \right) + \lambda \, Loss_{Jacobian} \right),$$

[**1**]

$$Loss_{Jacobian} = \sum_{i,j} \left(\frac{\partial h_j \left(\textbf{\textit{Env}}_{\textbf{\textit{reduced}}} \right)}{\partial \textbf{\textit{Env}}_{\textbf{\textit{reduced}}_i}} \right)^2.$$

[**2**]

After denoising with an autoencoder, we transformed the reconstructed 200-dimensional trial vectors back to the original space with the inverse PCA transformation. Notably, neither PCA nor the autoencoder had any information regarding the spatial locations of the electrodes. Finally, we low-passed each temporal trace with a cutoff frequency of 5 Hz for smoothing purposes.

Characterizing Spatiotemporal Patterns of Single-Trial Activities. The high-gamma amplitude envelopes from different electrode locations tended to amplify around movement initiation but at slightly different times. To quantify the exact time of amplification for a particular electrode, we took the first derivative of the smoothed denoised envelopes described above and took the time point of maximum within the canonical amplification window (-300 ms to 100 ms) as the amplification time, as long as that maximum exceeded the baseline mean by at least two baseline SDs (baseline was defined as $[-700$ ms, -400 ms] relative to movement onset). Once we computed those amplification times for different electrodes in a trial, we excluded outlier amplification times (outlier times is defined as times that deviated from the median time by more than six times of the median of the deviations). If there were more than 33% of electrodes left, we fit the amplification times for all electrodes (t_{amp}) with their x, y physical coordinates using linear regression (i.e., 2D planar fit). In Eq. 3, β_0 denotes the offset and β_1 and β_2 denote the coefficients for x, y axes. The direction of the propagation $\varphi_{propagation}$ is determined by the angle formed by the two coefficients (Eq. 4). The speed of the propagation $v_{propagation}$ is computed with Eq. 5 with the interelectrode distance $d_{interelec} = 0.4$ mm.

$$t_{amp} = \beta_0 + \beta_1 x + \beta_2 y, \qquad [3]$$

$$\varphi_{propagation} = \arctan\left(\frac{\beta_2}{\beta_1}\right), \qquad [4]$$

$$v_{propagation} = \left(\frac{1}{\sqrt{\beta_1^2 + \beta_2^2}}\right) \cdot d_{interelec}. \qquad [5]$$

The fit for each trial was evaluated based on the fraction of variance explained (i.e., R^2) of the linear regression ($R^2_{propagation}$). To determine whether the fit was statistically significant, we randomly shuffled electrode locations 500 times for each trial, pooled together the shuffled $R^2_{propagation}$ values from all trials and determined an overall $R^2_{propagation}$ threshold based on the top 5% cutoff of shuffled $R^2_{propagation}$ values. A trial with less than 33% of electrodes left for planar regression was automatically considered an insignificant trial.

Decoding Velocities with Spatiotemporal Patterns. This section explains the processes of evaluating whether the spatiotemporal propagating patterns could predict velocities.

For the *spatiotemporal model*, we used all parameters characterizing the spatiotemporal patterns ($v_{propagation}$, $sin(\varphi_{propagation})$, $cos(\varphi_{propagation})$, $R^2_{propagation}$), here bolded as they are now vectors from all trials) to predict the x and y components of the hand velocities (v_x, v_y), respectively, using a GLM with linear link and Gaussian family distribution. The formulation is identical to linear regressions, except that the solution is found with iteratively reweighted least squares method. In Eqs. 6 and 7, the m and l denote the medial and lateral arrays, respectively, while the x and y denote the x and y components of the velocity, respectively. A different model is computed for different timepoints with respect to movement onset from all trials, which is noted by t_i in the equations ($t_i \in [-200, 200]$ ms), so that we could determine when those spatiotemporal variables attained the best predictive power.

spatiotemporal model:

$$
\begin{aligned}
v_{x\_t_i} = &\ \beta_{c\_x\_t_i} + \beta_{sin\_x\_l\_t_i} sin\left(\varphi_{propagation\_l}\right) \\
&+ \beta_{cos\_x\_l\_t_i} cos\left(\varphi_{propagation\_l}\right) + \beta_{v\_x\_l\_t_i} v_{propagation\_l} \\
&+ \beta_{fit\_x\_l\_t_i} R^2_{propagation\_l} + \beta_{sin\_x\_m\_t_i} sin\left(\varphi_{propagation\_m}\right) \\
&+ \beta_{cos\_x\_m\_t_i} cos\left(\varphi_{propagation\_m}\right) + \beta_{v\_x\_m\_t_i} v_{propagation\_m} \\
&+ \beta_{fit\_x\_m\_t_i} R^2_{propagation\_m}
\end{aligned}
\qquad [6]
$$

$$
\begin{aligned}
v_{y\_t_i} = &\ \beta_{c\_y\_t_i} + \beta_{sin\_y\_l\_t_i} sin\left(\varphi_{propagation\_l}\right) + \beta_{cos\_y\_l\_t_i} cos\left(\varphi_{propagation\_l}\right) \\
&+ \beta_{v\_y\_l\_t_i} v_{propagation\_l} + \beta_{fit\_y\_l\_t_i} R^2_{propagation\_l} \\
&+ \beta_{sin\_y\_m\_t_i} sin\left(\varphi_{propagation\_m}\right) \\
&+ \beta_{cos\_y\_m\_t_i} cos\left(\varphi_{propagation\_m}\right) + \beta_{v\_y\_m\_t_i} v_{propagation\_m} \\
&+ \beta_{fit\_y\_m\_t_i} R^2_{propagation\_m}
\end{aligned}
\qquad [7]
$$

To obtain the *shuffle control model*, we randomly shuffled the hand velocities across trials and refitted the velocity prediction models.

All models were fit and evaluated with a 10-fold cross-validation scheme. We adapted the definition of R^2 and arrived at a composite fit measure $R^2_{v\_pred\_composite}$ for each pair of models, taking into account performances of v_x and v_y predictions simultaneously. In Eq. 8, $\hat{v_x}$ denotes the estimated v_x, while $\overline{v_x}$ denotes the average v_x (here suffix t_i is ignored from all variables for simplicity).

$$R^2_{v\_pred\_composite} = 1 - \frac{\sum\left((v_x - \hat{v_x})^2 + (v_y - \hat{v_y})^2\right)}{\sum\left((v_x - \overline{v_x})^2 + (v_y - \overline{v_y})^2\right)}. \qquad [8]$$

To compare the time-resolved performance of the *spatiotemporal model* versus the *shuffle control model*, we performed a single-tailed Wilcoxon test for the $R^2_{v\_pred\_composite}$ at the optimal time point for the *spatiotemporal model*.

Finally, to evaluate the relative importance of those spatiotemporal variables, we also computed reduced models that contained only a subset of the spatiotemporal propagating characteristics. For example, the *direction-only spatiotemporal model* only contained direction variables; the *speed-only spatiotemporal model* only contained speed variables; and the *fit-only spatiotemporal model* only contained R^2 variables. The rest is the same as described above with the *spatiotemporal model*.

direction-only spatiotemporal model (here, we wrote down only the formulations for the x component of the velocity for brevity; same below):

$$
\begin{aligned}
v_{x\_t_i} = &\ \beta_{c\_x\_t_i} + \beta_{sin\_x\_l\_t_i} sin\left(\varphi_{propagation\_l}\right) \\
&+ \beta_{cos\_x\_l\_t_i} cos\left(\varphi_{propagation\_l}\right) + \beta_{sin\_x\_m\_t_i} sin\left(\varphi_{propagation\_m}\right) \\
&+ \beta_{cos\_x\_m\_t_i} cos\left(\varphi_{propagation\_m}\right),
\end{aligned}
\qquad [9]
$$

speed-only spatiotemporal model:

$$v_{x\_t_i} = \beta_{c\_x\_t_i} + \beta_{v\_x\_l\_t_i} v_{propagation\_l} + \beta_{v\_x\_m\_t_i} v_{propagation\_m}, \qquad [10]$$

fit-only spatiotemporal model:

$$v_{x\_t_i} = \beta_{c\_x\_t_i} + \beta_{fit\_x\_l\_t_i} R^2_{propagation\_l} + \beta_{fit\_x\_m\_t_i} R^2_{propagation\_m}. \qquad [11]$$

Decoding Velocities with Envelopes and Spatiotemporal Patterns. To evaluate whether the spatiotemporal patterns contained additional information regarding kinematics that was nonredundant with what was contained in the high-gamma amplitude envelopes themselves, we built GLM models containing a) only the instantaneous amplitude envelopes ("*envelope-only model*"); b) only the spatiotemporal variables – including both first-order variables and second-order interactions ("*spatiotemporal-1stAnd2nd-only model*"); and c) both instantaneous amplitude envelopes and first- and second-order spatiotemporal variables ("*envelope+spatiotemporal1stAnd2nd model*").

The *envelope-only model* was lag-specific, meaning that we used instantaneous envelopes at a particular fixed lag to the hand velocities, to predict the hand velocities at all time points (0 ms to 200 ms w.r.t. movement onset) of all trials; the *envelope + spatiotemporal 1st And 2nd models* was also lag-specific given that it contained the instantaneous envelopes. The lags are denoted with Δt_i in the equations below ($\Delta t_i \in [-300, 100]$ ms).

In contrast, the *spatiotemporal-1stAnd2nd-only model* was not lag-specific, as only one set of spatiotemporal variables was computed for any given trial. The second-order interactions terms were constructed from the product of each pair of z-scored first-order spatiotemporal variables. The same model was also used to predict hand velocities of all time points (0 ms to 200 ms w.r.t. movement onset) of all trials, instead of only at a particular time point as was done in the previous section ("Decoding velocities with spatiotemporal patterns").

envelope-only model (where p denotes electrode number and Env denotes instantaneous amplitude envelope):

$$v_{x\_\Delta t_i} = \beta_{c\_x\_\Delta t_i} + \sum_{p=1}^{128} \beta_{env\_x\_\Delta t_i\_p} \cdot Env_p, \qquad [12]$$

$$v_{y\_\Delta t_i} = \beta_{c\_y\_\Delta t_i} + \sum_{p=1}^{128} \beta_{env\_y\_\Delta t_i\_p} \cdot Env_p. \quad [13]$$

spatiotemporal-1stAnd2nd-only model (where Spt_m denotes the m-th first-order spatiotemporal variable among a total of eight variables from both arrays, $\odot$ denotes element-wise product):

$$v_x = \beta_{c\_x} + \sum_{m=1}^{8} \beta_{spt\_x\_m} \cdot Spt_m + \sum_{m \neq n} \beta_{spt\_x\_m\_n} \cdot Spt_m \odot Spt_n, \quad [14]$$

$$v_y = \beta_{c\_y} + \sum_{m=1}^{8} \beta_{spt\_y\_m} \cdot Spt_m + \sum_{m \neq n} \beta_{spt\_x\_m\_n} \cdot Spt_m \odot Spt_n, \quad [15]$$

envelope+spatiotemporal1stAnd2nd model:

$$v_{x\_\Delta t_i} = \beta_{c\_x\_\Delta t_i} + \sum_{p=1}^{128} \beta_{env\_x\_\Delta t_i\_p} \cdot Env_p$$
$$+ \sum_{m=1}^{8} \beta_{spt\_x\_m} \cdot Spt_m + \sum_{m \neq n} \beta_{spt\_x\_m\_n} \cdot Spt_m \odot Spt_n, \quad [16]$$

$$v_{y\_\Delta t_i} = \beta_{c\_y\_\Delta t_i} + \sum_{p=1}^{128} \beta_{env\_y\_\Delta t_i\_p} \cdot Env_p$$
$$+ \sum_{m=1}^{8} \beta_{spt\_y\_m} \cdot Spt_m + \sum_{m \neq n} \beta_{spt\_x\_m\_n} \cdot Spt_m \odot Spt_n. \quad [17]$$

Except for the exact variables used in the model, all model specifications, numerical computations, cross-validation scheme, and composite performance measure were the same as the previous section "Decoding velocities with spatiotemporal patterns."

Afterward, we statistically tested whether the spatiotemporal variables added to the amplitude envelopes improved kinematic prediction. We first picked the best lag for the *envelope-only model* (i.e., the *envelope-only model* with the best mean $R^2_{v\_pred\_composite}$ across folds), then used the same lag for the *envelope+spatiotemporal1stAnd2nd model*. We compared the $R^2_{v\_pred\_composite}$ values obtained for both models with a single-tailed Wilcoxon test.

Last, we tested whether it was crucial to have the correct spatiotemporal variables corresponding to each trial to improve hand velocity prediction over the amplitude envelopes. For that, we randomly shuffled the spatiotemporal variables among trials 1,000 times, supplementing the correct instantaneous amplitude envelopes to predict hand velocities. Each shuffled prediction was fit and evaluated with a fourfold scheme; upon averaging across folds, it forms a $R^2_{v\_pred\_composite}$ distribution consisting of 1,000 samples. A top 5% threshold was determined from the distribution of shuffled $R^2_{v\_pred\_composite}$ values. We compared that threshold with the real $R^2_{v\_pred\_composite}$ from unshuffled spatiotemporal variables and amplitude envelopes after averaging across its 10 folds.

Code Availability. The code used for analyses in this study is available at https://github.com/hatsopoulos-lab/macaque-spatio_temporal_pattern.

Data, Materials, and Software Availability. Mat files data have been deposited in DRYAD (https://doi.org/10.5061/dryad.j6q573nj1) (30).

Author affiliations: [a]Committee on Computational Neuroscience, University of Chicago, Chicago, IL 60637; and [b]Organismal Biology and Anatomy, University of Chicago, Chicago, IL 60637

1. W. Penfield, E. Boldrey, Somatic motor and sensory representation in man. *Brain* **60**, 389–443 (1937).
2. M. C. Park, A. Belhaj-Saïf, P. D. Cheney, Properties of primary motor cortex output to forelimb muscles in rhesus macaques. *J. Neurophysiol.* **92**, 2968–2984 (2004).
3. K. Balasubramanian *et al.*, Propagating motor cortical dynamics facilitate movement initiation. *Neuron* **106**, 526–536.e4 (2020).
4. K. Balasubramanian, F. I. Arce-McShane, B. M. Dekleva, J. L. Collinger, N. G. Hatsopoulos, Propagating motor cortical patterns of excitability are ubiquitous across human and non-human primate movement initiation (2022). https://ssrn.com/abstract = 4108216.
5. R. D. Flint, E. W. Lindberg, L. R. Jordan, L. E. Miller, M. W. Slutzky, Accurate decoding of reaching movements from field potentials in the absence of spikes. *J. Neural. Eng.* **9**, 046006 (2012).
6. R. D. Flint, C. Ethier, E. R. Oby, L. E. Miller, M. W. Slutzky, Local field potentials allow accurate decoding of muscle activity. *J. Neurophysiol.* **108**, 18–24 (2012).
7. J. Zhuang, W. Truccolo, C. Vargas-Irwin, J. P. Donoghue, Decoding 3-D reach and grasp kinematics from high-frequency local field potentials in primate primary motor cortex. *IEEE Trans. Biomed. Eng.* **57**, 1774–1784 (2010).
8. S. Rifai, P. Vincent, X. Muller, X. Glorot, Y. Bengio, "Contractive auto-encoders: Explicit invariance during feature extraction" in *Proc. 28th Int. Conf. Mach. Learn. ICML 2011* (Omnipress, 2011), pp. 833–840.
9. R. D. Flint, Z. A. Wright, M. R. Scheid, M. W. Slutzky, Long term, stable brain machine interface performance using local field potentials and multiunit spikes. *J. Neural Eng.* **10**, 056005 (2013).
10. J. Y. Wu, X. Huang, C. Zhang, Propagating waves of activity in the neocortex: What they are, what they do. *Neuroscientist* **14**, 487–502 (2008).
11. T. K. Sato, I. Nauhaus, M. Carandini, Traveling waves in visual cortex. *Neuron* **75**, 218–229 (2012).
12. T. P. Zanos, P. J. Mineault, K. T. Nasiotis, D. Guitton, C. C. Pack, A sensorimotor role for traveling waves in primate visual cortex. *Neuron* **85**, 615–627 (2015).
13. W. Xu, X. Huang, K. Takagaki, J. YoungWu, Compression and reflection of visually evoked cortical waves. *Neuron* **55**, 119–129 (2007).
14. E. V. Lubenov, A. G. Siapas, Hippocampal theta oscillations are travelling waves. *Nature* **459**, 534–539 (2009).
15. J. Patel, S. Fujisawa, A. Berényi, S. Royer, G. Buzsáki, Traveling theta waves along the entire septotemporal axis of the hippocampus. *Neuron* **75**, 410–417 (2012).
16. M. Besserve, S. C. Lowe, N. K. Logothetis, B. Schölkopf, S. Panzeri, Shifts of gamma phase across primary visual cortical sites reflect dynamic stimulus-modulated information transfer. *PLoS Biol.* **13**, 1–29 (2015).
17. L. Muller, A. Destexhe, Propagating waves in thalamus, cortex and the thalamocortical system: Experiments and models. *J. Physiol. Paris* **106**, 222–238 (2012).
18. I. Nauhaus, L. Busse, D. L. Ringach, M. Carandini, Robustness of traveling waves in ongoing activity of visual cortex. *J. Neurosci.* **32**, 3088–3094 (2012).
19. A. Gabriel, R. Eckhorn, A multi-channel correlation method detects traveling γ-waves in monkey visual cortex. *J. Neurosci. Methods* **131**, 171–184 (2003).
20. Z. Pang, A. Alamia, R. Vanrullen, Turning the stimulus on and off changes the direction of α traveling waves. *eNeuro* **7**, 1–11 (2020).
21. U. R. Mohan, H. Zhang, J. Jacobs, The direction and timing of theta and alpha traveling waves modulate human memory processing. bioRxiv [Preprint] 2022.02.07.479466 (2022). https://doi.org/10.1101/2022.02.07.479466 (Accessed 10 February 2022).
22. D. Rubino, K. A. Robbins, N. G. Hatsopoulos, Propagating waves mediate information transfer in the motor cortex. *Nat. Neurosci.* **9**, 1549–1557 (2006).
23. K. Takahashi *et al.*, Large-scale spatiotemporal spike patterning consistent with wave propagation in motor cortex. *Nat. Commun.* **6**, 1–11 (2015).
24. Z. W. Davis, L. Muller, J. Martinez-Trujillo, T. Sejnowski, J. H. Reynolds, Spontaneous travelling cortical waves gate perception in behaving primates. *Nature* **587**, 432–436 (2020).
25. M. T. Kaufman *et al.*, The largest response component in the motor cortex reflects movement timing but not movement type. *eNeuro* **3**, 1–25 (2016).
26. N. I. Fisher, T. Lewis, B. J. J. Embleton, *Statistical Analysis of Spherical Data* (Cambridge University Press, 1993).
27. S. R. Jammalamadaka, A. Sengupta, *Topics in Circular Statistics* (World Scientific, 2001), vol. **5**.
28. J. H. Zar, *Biostatistical Analysis*. Fifth ed. 960 (Prentice Hall, 2009).
29. P. Berens, CircStat: A MATLAB Toolbox for Circular Statistics. *J. Stat. Softw.* **31**, 1–21 (2009).
30. N.G. Hatsopoulos, W. Liang, K. Balasubramanian, V. Papadourakis, Propagating spatio-temporal activity patterns across macaque motor cortex carry kinematic information, Dryad, Dataset, (2022) https://doi.org/10.5061/dryad.j6q573nj1.